



PAPER

 View Article Online
View Journal | View Issue
Cite this: *RSC Adv.*, 2018, 8, 39769

Self-standing $\text{Li}_{1.2}\text{Mn}_{0.6}\text{Ni}_{0.2}\text{O}_2$ /graphene membrane as a binder-free cathode for Li-ion batteries†

 Yang Puheng, Wang Wenxu, Zhang Xiaoliang,  Li Honglei, Zhang Shichao * and Xing Yalan*

Lithium-rich transition-metal layered oxides (LROs), such as $\text{Li}_{1.2}\text{Mn}_{0.6}\text{Ni}_{0.2}\text{O}_2$, are promising cathode materials for application in Li-ion batteries, but the low initial coulombic efficiency, severe voltage fade and poor rate performance of the LROs restrict their commercial application. Herein, a self-standing $\text{Li}_{1.2}\text{Mn}_{0.6}\text{Ni}_{0.2}\text{O}_2$ /graphene membrane was synthesized as a binder-free cathode for Li-ion batteries. Integrating the graphene membrane with $\text{Li}_{1.2}\text{Mn}_{0.6}\text{Ni}_{0.2}\text{O}_2$ forming a $\text{Li}_{1.2}\text{Mn}_{0.6}\text{Ni}_{0.2}\text{O}_2$ /graphene structure significantly increases the surface areas and pore volumes of the cathode, as well as the reversibility of oxygen redox during the charge–discharge process. The initial discharge capacity of the $\text{Li}_{1.2}\text{Mn}_{0.6}\text{Ni}_{0.2}\text{O}_2$ /graphene membrane is $\sim 270 \text{ mA h g}^{-1}$ ($\sim 240 \text{ mA h g}^{-1}$ for $\text{Li}_{1.2}\text{Mn}_{0.6}\text{Ni}_{0.2}\text{O}_2$) and its initial coulombic efficiency is 90% (72% for $\text{Li}_{1.2}\text{Mn}_{0.6}\text{Ni}_{0.2}\text{O}_2$) at a current density of 40 mA g^{-1} . The capacity retention of the $\text{Li}_{1.2}\text{Mn}_{0.6}\text{Ni}_{0.2}\text{O}_2$ /graphene membrane remains at 88% at 40 mA g^{-1} after 80 cycles, and the rate performance is largely improved compared with that of the pristine $\text{Li}_{1.2}\text{Mn}_{0.6}\text{Ni}_{0.2}\text{O}_2$. The improved performance of the $\text{Li}_{1.2}\text{Mn}_{0.6}\text{Ni}_{0.2}\text{O}_2$ /graphene membrane is ascribed to the lower charge-transfer resistance and solid electrolyte interphase resistance of the $\text{Li}_{1.2}\text{Mn}_{0.6}\text{Ni}_{0.2}\text{O}_2$ /graphene membrane compared to that of $\text{Li}_{1.2}\text{Mn}_{0.6}\text{Ni}_{0.2}\text{O}_2$. Moreover, the lithium ion diffusion of the $\text{Li}_{1.2}\text{Mn}_{0.6}\text{Ni}_{0.2}\text{O}_2$ /graphene membrane is enhanced by three orders of magnitude compared to that of $\text{Li}_{1.2}\text{Mn}_{0.6}\text{Ni}_{0.2}\text{O}_2$. This work may provide a new avenue to improve the electrochemical performance of LROs through tuning the oxygen redox progress during cycling.

 Received 18th July 2018
Accepted 31st October 2018

DOI: 10.1039/c8ra06086j

rsc.li/rsc-advances

Introduction

Li-ion batteries are becoming increasingly important as a power source supplying for electric vehicles (EVs). However, for commercial Li-ion batteries challenges remain to be met with the power demands of EVs with driving ranges of more than 300 miles due to low specific capacities of commercial cathode materials, such as $\text{LiNi}_{1/3}\text{Mn}_{1/3}\text{Co}_{1/3}\text{O}_2$ ($< 200 \text{ mA h g}^{-1}$) and LiFeO_4 (170 mA h g^{-1}). Lithium-rich transition-metal oxide (LRO) is a promising cathode material due to its high specific capacity ($> 250 \text{ mA h g}^{-1}$) and average operating potential.^{1–4} A LRO material with notation $x\text{Li}_2\text{MnO}_3 \cdot (1-x)\text{LiMO}_2$ ($\text{M} = \text{Mn}, \text{Ni}, \text{Co}, \text{etc.}$) generally consists of rhombohedral LiMO_2 and monoclinic Li_2MnO_3 . Although LiMO_2 and Li_2MnO_3 are layered NaFeO_2 -type rock salt structures, Li_2MnO_3 can be written as $\text{Li}(\text{Li}_{1/3}\text{Mn}_{2/3})\text{O}_2$, which means that the sites in Mn layers can be occupied by Li ions, reducing symmetry of Li_2MnO_3 to the $C2/c$

space group.^{5,6} The high reversible capacities of these materials are believed to be associated with the O^{2-}/O^- redox process in bulk regions of LRO particles.^{7,8} Whereas the O_2 release process accompanied by O^{2-} oxidation during the first charge of LROs, results in negative consequences such as migration of the transition metal,⁹ surface reconstruction,¹⁰ and micro cracks along grain boundaries,¹¹ leading to low initial coulombic efficiency, severe voltage fade and poor rate performance. Therefore, LROs working as cathode materials face challenges in order to be commercialized for application in Li-ion batteries.^{12–15}

To overcome the above drawbacks of the LROs, extensive studies have been carried out in the past few years. Song *et al.*¹⁶ and Liu *et al.*¹⁷ modified the surface of $\text{Li}_{1.2}\text{Mn}_{0.54}\text{Ni}_{0.13}\text{Co}_{0.13}\text{O}_2$ (LLMNC) particles with spinel phase to increase the coulombic efficiency and lower the resistance. Li *et al.* improved initial coulombic efficiency of $\text{Li}_{1.2}\text{Mn}_{0.6}\text{Ni}_{0.2}\text{O}_2$ through Ba^{2+} doping and obtained better rate performance.¹⁸ Qing *et al.* doped the LLMNC with Na^+ using molten-salt method to increase the electronic and ionic conductivity of LLMNC and therefore notably enhancing electrochemical performance.¹⁹ These works proved that improving Li^+ diffusion in cathode is an effective method to optimize the electrochemical performance of the

School of Materials Science and Engineering, Beihang University, Beijing 100191, PR China. E-mail: csc@buaa.edu.cn; xingyalan@buaa.edu.cn; Fax: +86 01082338148; Tel: +86 01082339319

† Electronic supplementary information (ESI) available. See DOI: 10.1039/c8ra06086j



LROs. Carbon based materials can be applied to promote electrochemical kinetics of cathode materials due to their chemically stable and excellent electronic transport properties.^{20–22} Among the carbon based materials, graphene nanosheets have attracted tremendous attentions on account of high surface area, low weight, and high mechanical strength.^{23–26} However, combining the $\text{Li}_{1.2}\text{Mn}_{0.6}\text{Ni}_{0.2}\text{O}_2$ with graphene membrane, which may not only increase the electrochemical kinetics of the electrodes, but also provide freestanding structure without any inactive mechanical support, has not been studied.

In this work, the self-standing $\text{Li}_{1.2}\text{Mn}_{0.6}\text{Ni}_{0.2}\text{O}_2$ /graphene membrane was synthesized *via* vacuum filtration to apply as a cathode material in Li-ion battery. The $\text{Li}_{1.2}\text{Mn}_{0.6}\text{Ni}_{0.2}\text{O}_2$ /graphene membrane has a large specific surface area, and also exhibits good electrochemical properties. At the current density of 40 mA g^{-1} (0.2C), its initial discharge capacity is 278 mA h g^{-1} and coulombic efficiency is up to 90%, which is much higher than that of the pristine $\text{Li}_{1.2}\text{Mn}_{0.6}\text{Ni}_{0.2}\text{O}_2$. Rate capacity of the membrane is also significantly improved compared with that of the pristine $\text{Li}_{1.2}\text{Mn}_{0.6}\text{Ni}_{0.2}\text{O}_2$. The cause of increased initial coulombic efficiency was studied by extensive techniques, which shows that the better oxygen redox reversibility during the first cycle for the membrane plays a crucial role in the enhancement of electrochemical performance of $\text{Li}_{1.2}\text{Mn}_{0.6}\text{Ni}_{0.2}\text{O}_2$ /graphene membrane. This work could provide a new avenue to improve the electrochemical performance of the LROs through tuning the reversibility of oxygen redox during the charge–discharge processes.

Experimental

Materials synthesis

All reagents are analytical grade and used as-purchased without any purification.

Synthesis of $\text{Li}_{1.2}\text{Mn}_{0.6}\text{Ni}_{0.2}\text{O}_2$ by an inverse microemulsion route

Moderate amounts of lithium dodecyl sulphate ($\text{C}_{12}\text{H}_{25}\text{LiO}_4\text{S}$, Macklin) and *n*-butanol ($\text{CH}_3(\text{CH}_2)_3\text{OH}$, Macklin) were dissolved in cyclohexane (C_6H_{12} , Macklin) under stirring to form the oil phase (marked as solution A). Solution A was divided into two equal parts (marked as A1 and A2). Stoichiometric amounts of manganese nitrate ($\text{Mn}(\text{NO}_3)_2 \cdot 4\text{H}_2\text{O}$, Macklin) and nickel nitrate ($\text{Ni}(\text{NO}_3)_2 \cdot 6\text{H}_2\text{O}$, Macklin) were dissolved in deionized water (H_2O) to get a transparent solution (marked as B1). Appropriate amounts of sodium hydroxide (NaOH , Macklin) and ammonium hydroxide ($\text{NH}_3 \cdot \text{H}_2\text{O}$, Macklin) were dissolved in deionized water (H_2O) to get a transparent solution (marked as B2). The emulsions C1 and C2 were prepared by adding solution B1 and B2 into A1 and A2 under stirring for 12 h at ambient condition, respectively. Emulsion C1 was mixed with emulsion C2 under magnetic stirring, the mixed solution was filtered and washed several times to get brown slurry. As-obtained slurry was dried at 80°C in blast drying oven, and then blended with lithium nitrate (LiNO_3 , Macklin) thoroughly under grinding. The mixture was heated at 350°C for 4 h with

subsequent sintering at 900°C for 15 h. Brownish black coloured $\text{Li}_{1.2}\text{Mn}_{0.6}\text{Ni}_{0.2}\text{O}_2$ powder samples were obtained (marked as LMR).

Synthesis of $\text{Li}_{1.2}\text{Mn}_{0.6}\text{Ni}_{0.2}\text{O}_2$ /graphene membrane

Appropriate amounts of LMR, commercial graphene sheet (Aladdin) and polyvinyl pyrrolidone (Aladdin) (LMR : graphene : PVP = 8 : 2 : 1 in weight) were dispersed into ethylene glycol ($(\text{CH}_2\text{OH})_2$, Macklin) by sonication for 1 h. Then the mixture of LMR and graphene was filtrated with vacuum pump using a nylon membrane. After washing with deionized water and ethyl alcohol several times and dried at 60°C for 5 h, the hybrid membrane was pressed at 0.5 MPa and peeled from the filter membrane with subsequent drying at 150°C for 4 h to get the LMR/graphene membrane (marked as LMR/G). The membrane with LMR : graphene = 7 : 3 was also prepared, marked as LMR/G-30.

Materials characterization

The crystal structures of the as-prepared materials were characterized through X-ray diffraction (XRD, Rigaku D/Max-2400, Japan) with $\text{Cu K}\alpha$ ($\lambda = 1.5418 \text{ \AA}$) radiation at 40 kV and 40 mA at a scanning rate of 1° min^{-1} within 2 theta range of $10\text{--}80^\circ$. The Li, Mn, and Ni content in LMR was analyzed using an inductively coupled plasma-atomic emission spectrometer (ICP-AES, Agilent 7500ce, USA). The oxidation valence states and element content of the metal elements at the surface regions were determined by X-ray photoelectron spectroscopy (XPS, Thermo escalab 250Xi, USA). Raman spectroscopy (Raman, LabRam HR800, Japan) was collected with 1.96 eV (632.8 nm) excitation laser. Thermal gravimetric analysis (TG, NETZSCH STA 449C, Germany) for LMR/graphene membrane was recorded from room temperature to 900°C at a heating rate of $10^\circ\text{C min}^{-1}$ in air. The morphologies of materials were observed by scanning electron microscopy (SEM, Hitachi S-4800, Japan) and transmission electron microscopy (TEM, FEI Tecnai G2 F30, Japan). The surface areas and porosities were measured by the Brunauer–Emmett–Teller (BET, Quantachrome Autosorb-1C-VP, USA) method with N_2 adsorption–desorption isotherms.

Electrochemical measurements

Electrodes of LMR were prepared by mixing LMR (80 wt%), Super P (10 wt%), and PVDF (10 wt%) in a mortar and milled for half an hour, and then several drops of *N*-methyl-2-pyrrolidone (NMP) were added into the mixture with continuously stirring. The obtained slurry was uniformly dispersed and spread on aluminum foils current collectors with the mass loading for around 2 mg cm^{-2} . After dried in a vacuum oven at 100°C for 2 h, the aluminum foil with LMR was pressed under a pressure of 8 MPa to gain the single-sided cathode.

2032-type cells were assembled by as-prepared cathode or LMR/graphene as cathode, lithium plate used as the anode, Celgard 2400 as the separator, $1 \text{ mol L}^{-1} \text{ LiPF}_6$ in ethylenecarbonate/diethyl carbonate/dimethyl carbonate



(volume ratio of 1 : 1 : 1) as the electrolyte in an argon-filled glove box.

Electrochemical performances were tested by LAND CT2001A test system (Galvanostatic discharge/charge, 2.0–4.8 V vs. Li^+/Li , room temperature), and Zahner IM6e electrochemical workstation (Electrochemical impedance spectra, EIS, 1 MHz to 0.1 Hz, all cells were charged to 4.2 V before EIS test).

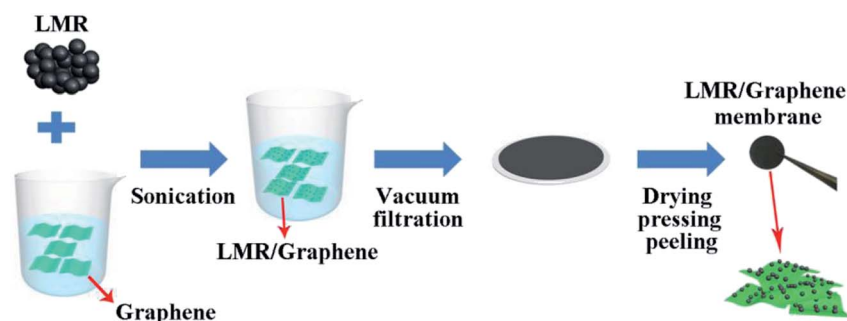
Results and discussion

Scheme 1 schematically presents the fabrication processes of the LMR/G. LMR/G was gained through sonication and vacuum filtration method. Fig. 1a shows the XRD patterns of LMR, LMR/G and LMR/G-30, and the graphene was also plotted for comparison. All peaks of the LMR with strong intensity can be well indexed to the O3 type NaFeO_2 layered structure (space group $R\bar{3}m$). The peaks with slightly lower intensity in the range of 20–25° can be indexed to monoclinic Li_2MnO_3 (space group $C2/m$), known as the characteristic peaks of Li-rich phase.^{27–29} None of any impurity phases was detected in the XRD pattern, indicating that there were no any trace amounts of impurity in LMR. Splitting peaks at 38° (006/012) and 65° (108/110) in the XRD pattern suggest the layered hexagonal structure was successfully obtained. Meanwhile, the ratio of $I(003)/I(104)$ is 1.31 for LMR that is higher than 1.2, showing a good order between Li and transition metal layers.^{30,31} As for LMR/G and LMR/G-30, the majority amount of the peaks in the XRD pattern

matched well with the characteristic peaks of LMR, except the peaks at 26° and 55° indicated by (002) and (004) plane diffraction of graphene, respectively.^{32,33} Comparing with LMR/G, the ratio of $I(003)/I(004)$ for LMR/G-30 is slightly lower, and this is owing to the higher graphene content in LMR/G-30. To further confirm the structure of as-prepared materials, the Raman spectra was measured for the LMR and LMR/G, as shown in Fig. 1b. For both materials, three distinct peaks at 608, 494 and 440 cm^{-1} can be assigned to ν_{MO_6} vibration ($M = \text{Ni}, \text{Mn}$ cations, A_{1g} mode), $\delta_{\text{O-M-O}}$ vibration (E_g mode) of $R\bar{3}m$ space group and short-range superlattice of Li_2MnO_3 -like $C2/m$ space group, respectively.^{34–36} LMR/G shows three peaks attributed to D, G and 2D bands of graphene at 1340, 1583 and 2680 cm^{-1} , respectively. Low intensity of the D band ($I_G : I_D = 4.4$) is owing to little defects existing in the graphene of LMR/G.^{37,38}

To obtain more information concerning the composition of LMR, ICP-AES technique was employed. The atomic ratios of $\text{Li} : \text{Mn} : \text{Ni}$ is 1.208 : 0.604 : 0.204 for LMR, which is very close to the target composition ($\text{Li}_{1.2}\text{Mn}_{0.6}\text{Ni}_{0.2}\text{O}_2$).

Fig. 2 and S2† shows the SEM image of LMR, LMR/G and LMR/G-30, respectively. It can be seen that the LMR has a particle size of 100–300 nm (Fig. 2a). For the LMR/G, the thickness of the LMR/G membrane is about 60 μm (Fig. 2b), and the LMR particles homogeneously disperse on the surface of graphene sheets, significantly increasing the dispersity of LMR comparing with that of LMR (Fig. S3†) applied as cathode. For the LMR/G-30, the thickness is about 80 μm . To characterize the



Scheme 1 Schematic of the fabrication processes of LMR/graphene membrane.

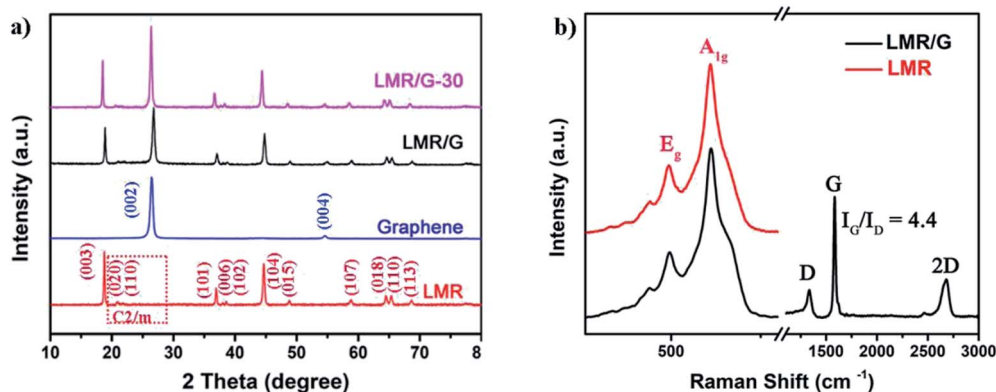


Fig. 1 (a) XRD of LMR, LMR/G and LMR/G-30. (b) Raman patterns of LMR and LMR/G.



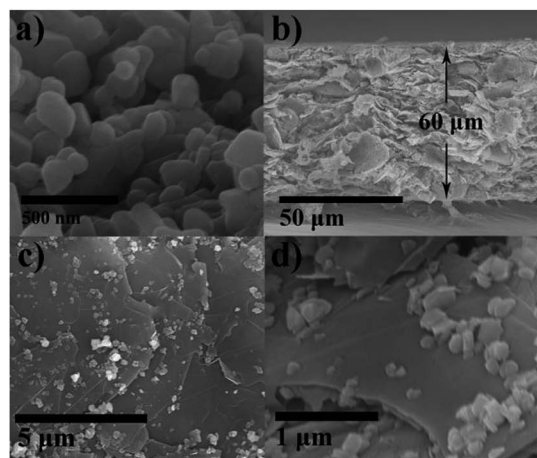


Fig. 2 (a) SEM images of LMR. (b) Cross-sectional SEM image of LMR/G membrane. (c) Top view low-magnification and (d) high-magnification SEM of LMR/G membrane.

distribution of the elements, scanning electron microscopy-energy dispersive spectrometer (SEM-EDS) method and the corresponding elemental mapping of LMR/G were adopted, as shown in Fig. S4.† The elemental maps of Mn, Ni, C and O demonstrate a uniform distribution. The BET surface area (shown in Fig. S5†) is 21.8 and 4.8 m² g^{−1} for LMR/G and LMR, respectively, which is attributed to the introduction of graphene membrane. The pores volumes of LMR/G (0.115 cm³ g^{−1}) is also enhanced compared to that of the LMR (0.031 cm³ g^{−1}), benefiting electrolyte contacting. The thermogravimetry was studied for both LMR and LMR/G (Fig. S6†), which shows that ~19.4% mass loss occurred from 430 to 700 °C for LMR/G, ascribing to the oxidization of graphene. These results suggest that the mass percentage of graphene in the LMR/G is 19.4%.³⁹

Fig. S7† shows the TEM images of LMR, according to Fig. S7a and b,† LMR particles are sub-micron with particle size of 100–300 nm, agreeing well with SEM images. The boundaries between particles are legible, indicating that the particles stack together rather than aggregate, and the particles are easier to segregate during the ultrasonic process. HRTEM images and corresponding Fast Fourier Transform images of LMR are exhibited in Fig. S7c and d,† according with the (104) and (003) planes of *R3m* structure, respectively. Fig. 3 shows the TEM images of LMR/G, which reveals that the graphene sheet overlaps with each other to form the graphene membrane, and LMR particles disperse uniformly in the graphene sheets. The LMR particles with size of 60–100 nm loads on the graphene sheets and tightly combines with graphene sheets (Fig. 3b). The high-resolution TEM image of the regions inside the dotted red square in Fig. 3c is exhibited in Fig. 3d, and the visible lattice fringes with a crystalline interplanar spacing of 0.47 nm, which is assigned to the (003) planes of the *R3m* structure, overlapping with lattice fringes of graphene (shown in dotted red circle of Fig. 3d).⁴⁰

The XPS spectra of pristine LMR and LMR/G are shown in Fig. 4. The O 1s spectrum of LMR with two peaks at 529.5 and 531.6 eV corresponding to O^{2−} anions belonged to the crystalline network and corresponded to weakly adsorbed surface species, respectively,⁴¹ while the weak single at 533.4 eV is attributed to defective sites of graphene.⁴² The oxidation states of Mn were deduced from Mn 3s core levels, splitting into a doublet. The separation between the two peaks of the doublet (ΔE_{3s}), which is sensitive to the oxidation states of Mn (O_{Mn}), can be estimated from eqn (1).^{43–45}

According to eqn (1), O_{Mn} is about 4 for LMR and LMR/G, implying that few oxygen vacancies existed on the surface of

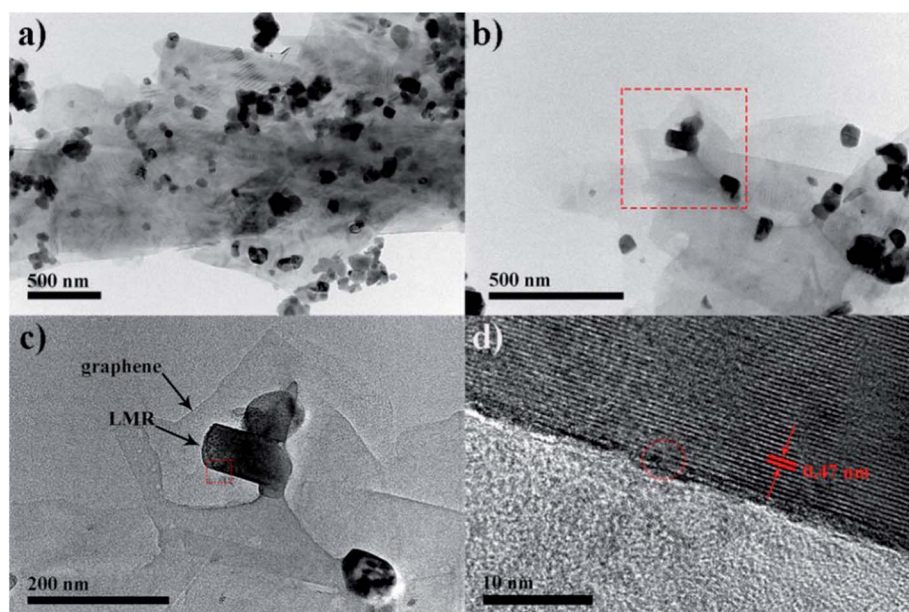


Fig. 3 (a) Low-magnification TEM image of LMR/G. (b) TEM image of LMR/G in the selected area in (a). (c) high-magnification TEM image of LMR/G, selected area in (b). (d) HRTEM image of LMR/G marked in (c).



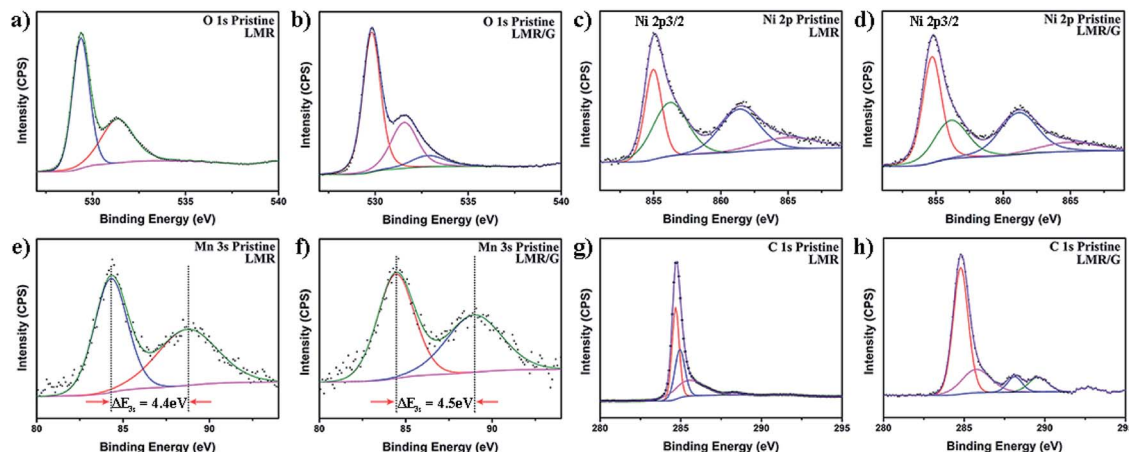


Fig. 4 Core-level XPS spectra of O 1s for (a) LMR and (b) LMR/G. Core-level XPS spectra of Ni 2p for (c) LMR and (d) LMR/G. Core-level XPS spectra of Mn 3s for (e) LMR and (f) LMR/G. Core-level XPS spectra of C 1s for (g) LMR and (h) LMR/G.

both samples.⁴⁶ Ni element on the surface of both materials is Ni^{2+} in the majority with minor amount of Ni^{3+} .⁴⁷

$$O_{\text{Mn}} = 9.67 - 1.27 \times \Delta E_{3s} \quad (1)$$

As shown in the C 1s spectra (Fig. 4g and h), the bonding energies of 284.6 and 285.5 eV for LMR can be assigned to C-C and C-OH functional groups, while the bonding energies of 288 and 289.7 eV for LMR/G is attributed to C=O and C=O-OH

bonds, respectively, indicating the presence of defects on the surfaces of graphene in LMR/G.⁴⁸

Fig. 5a and S8† shows the initial charge-discharge curves of LMR, LMR/G and LMR/G-30 at 20 mA g⁻¹ (0.1C), respectively. For all materials, the initial curves exhibit a comparable shape. Specifically, the sloping region below 4.5 V is attributed to the oxidation of Ni^{2+} , while the plateau region at around 4.5 V can be assigned to the oxidation of O^{2-} during the initial charge

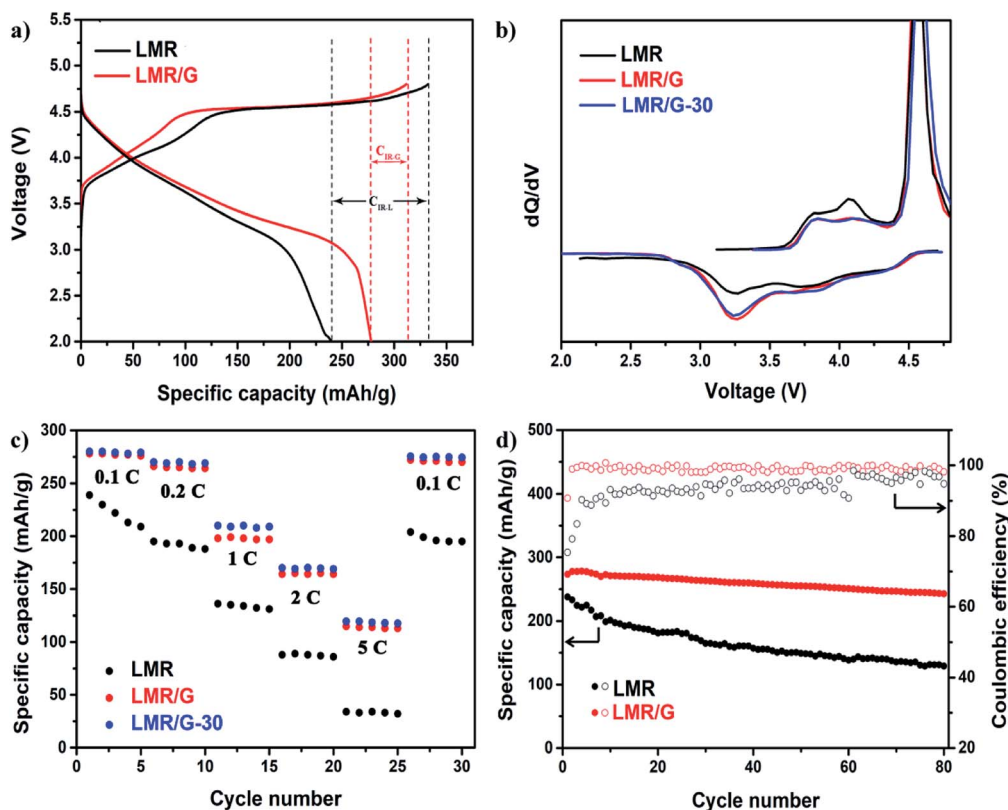


Fig. 5 (a) Charge and discharge curves of LMR and LMR/G during the first cycle at 0.1C. (b) dQ/dV plots of all materials during the first cycle at 0.1C. (c) Rate property of all materials at 0.1C, 0.2C, 1C, 2C, 5C and back to 0.1C. (d) Cycling performance of LMR and LMR/G at 0.2C. (1C = 200 mA g⁻¹).

process, and the sloping region is ascribed to the reduction of Ni^{4+} and O^- during the initial discharge process.^{49,50} The irreversible specific capacities is 92 and 33 mA h g^{-1} for LMR and LMR/G, respectively, thus increasing the initial coulombic efficiency from 72% ($240/332 \text{ mA h g}^{-1}$) to 90% ($278/311 \text{ mA h g}^{-1}$) as the formation of LMR/G membrane. As for LMR/G-30, the initial coulombic efficiency is 89% ($280/313 \text{ mA h g}^{-1}$), similar to that of LMR/G. To further study the electrochemical process during the first cycle, dQ/dV plots were adopted in Fig. 5b. Two oxidation peaks from 3.8 to 4.1 V and the sharp oxidation peak at around 4.5 V are attributed to the oxidation of Ni element from Ni^{2+} to Ni^{4+} and O^{2-} , respectively, corresponding to initial charge curve in Fig. 5a. The main difference between LMR and the membrane cathodes during initial discharge process is the reduction peak at 3.25 V, which is assigned to the reduction of O^- .⁴⁹ Reduction peak of O^- is much stronger for LMR/G and LMR/G-30 than LMR, and this is the source where LMR/G and LMR/G-30 have more reversible capacity than LMR. Indeed, there were several works using graphene and/or carbon nanotube as additive in LROs, but they were less effective in improving the initial coulombic efficiency without any post treatment (shown in Table S1†). Rate properties and relative voltage profiles for the materials are shown in Fig. 5c and S9,† respectively. Discharge capacities of LMR, LMR/G and LMR/G-30 at 0.1C, 0.2C, 1C, 2C and 5C are listed in Table S2,† compared with LMR, the membrane cathode deliver much high discharge capacities at large current densities. The discharge capacity of LMR/G-30 is slightly higher than that of LMR/G at each current density. Cycle performance at 0.2C during 80 cycles for LMR and LMR/G is shown in Fig. 5d. As is seen, coulombic efficiency of LMR/G remains above 98% after the initial cycle and the discharge capacity retains 242 mA h g^{-1} after 80 cycles (88% of the initial discharge capacity), while coulombic efficiency of LMR shows significant fluctuations ranging from 90% to 99% during cycling (after the third cycle) and the discharge capacity is only 130 mA h g^{-1} at the end of cycling. Discharge capacities of all samples at 1C during 100 cycles are exhibited in Fig. S10.† The initial discharge capacity of LMR, LMR/G and LMR/G-30 is 138, 192 and 202 mA h g^{-1} , respectively. After 100 times cycling, the capacity retention ratios of the membrane cathodes are above 90%, and it is 85% for LMR.

As shown in Fig. 6a, the EIS tests were performed to investigate the effect of graphene membrane on resistances and Li^+ ions diffusion of LMR. The EIS data were fitted by program 'ZSimpwin', and the equivalent circuit plot is shown on the left in Fig. 6a. For all materials, the high frequency intercept at the Z' axis is the resistances rooted in the electrolyte and other cell components (R_e). The high frequency semicircle is relevant to the solid electrolyte interphase resistance (R_{SEI}) and the middle frequency semicircle is relevant to the charge-transfer resistance (R_{ct}) at the surface region of the electrode. The low-frequency tail can be described as the Warburg impedance (W_o).⁵¹ The fitting results are listed in Table S3,† compared to LMR, R_e of the membrane cathodes remain unchanged at about 4Ω , while R_{SEI} and R_{ct} decreases significantly, total resistances ($R = R_e + R_{\text{SEI}} + R_{\text{ct}}$) of LMR/G and LMR/G-30 are much less than

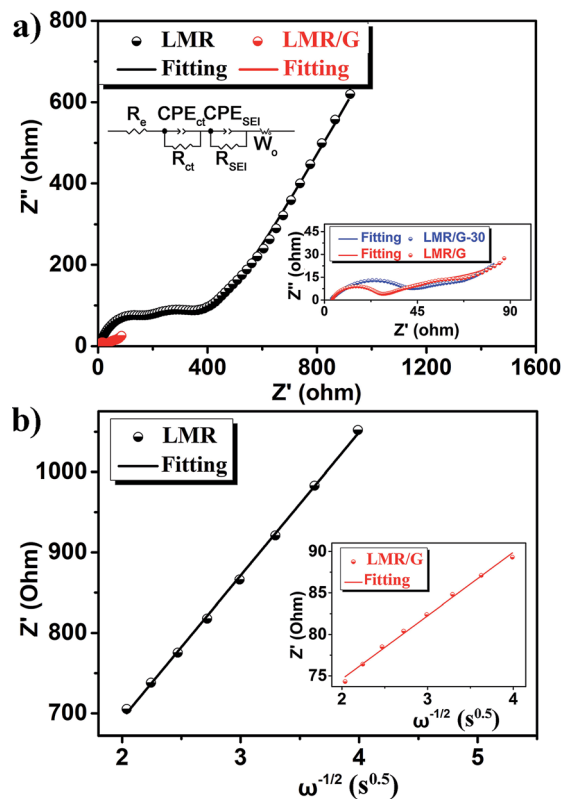


Fig. 6 (a) EIS spectra of half-cells of all materials charged to 4.2 V during the first cycle. (b) Profiles of Z' vs. $\omega^{-1/2}$ at low frequency.

that of LMR, indicating LMR/G has faster Li^+ -deintercalation kinetics. Total resistance of LMR/G-30 is 71Ω , lower than that of LMR/G (76Ω), this may be benefitted from better conductivity with higher graphene content.

Li^+ diffusion coefficients (D_{Li^+}) were calculated by eqn (2):⁵²

$$D_{\text{Li}^+} = 0.5R^2T^2/n^4A^2F^4C^2\sigma^2 \quad (2)$$

The Warburg factor σ is the slope of linear fitting of Z' vs. $\omega^{-1/2}$, Fig. 6b presents the plots of Z' vs. $\omega^{-1/2}$ in low frequency for LMR and LMR/G, and the value of D_{Li^+} for LMR/G and LMR is 1.03×10^{-14} and 2.34×10^{-17} , respectively. D_{Li^+} of LMR/G is three orders of magnitude higher than that of LMR, indicating that the electrode kinetics improve markedly with the introduction of graphene membrane.

To reveal principle of the significant coulombic efficiency increasing during the first cycle, the O 1s XPS spectra of initial charged LMR and LMR/G at 0.1C were exhibited in Fig. 7. Compared to the spectra of pristine LMR/G, the peak at 529.5 eV became weaker and a new peak appeared at around 530 eV (corresponding to O^- species) for the initial charged LMR/G, which indicates that the crystalline framework of O remains at the surface area of LMR/G during charge process.⁵³ However, the peak at 529.5 eV nearly disappears and no peak emerges after the initial charge for LMR, which can be attributed to severe side reaction arising from the loss of lattice oxygen from the surface region, detrimental to the reversibility of redox process.⁵⁴



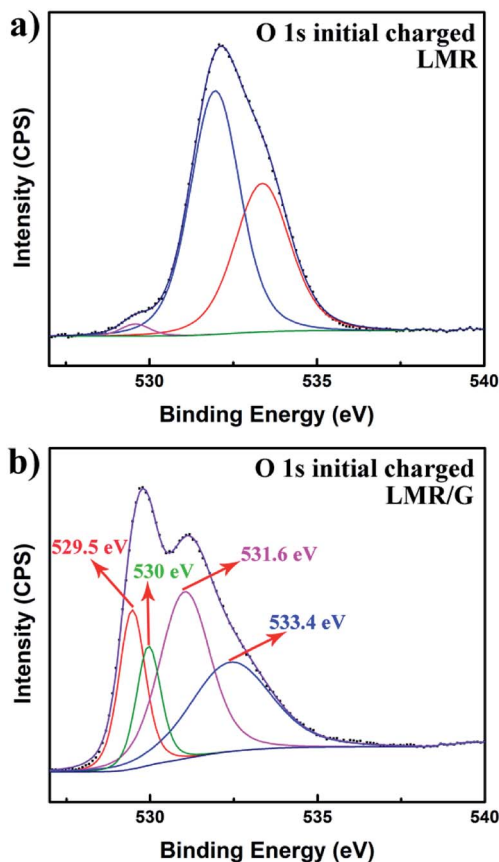


Fig. 7 Core-level XPS spectra of O 1s for (a) LMR and (b) LMR/G after the first charge progress.

Conclusions

In summary, the self-standing $\text{Li}_{1.2}\text{Mn}_{0.6}\text{Ni}_{0.2}\text{O}_2$ /graphene membrane was successfully synthesized as the cathode electrode for Li-ion batteries. LMR particles were uniform dispersive on the graphene membrane that significantly increased the surface areas and pore volume of LMR comparing with that of pristine LMR. The reversibility of oxygen redox of LMR/G was largely improved during the first cycle compared to that of LMR, leading to the higher discharge capacities of LMR/G than that of LMR. Meanwhile, the rate performance optimized with Li^+ diffusion coefficients increased by three orders of magnitude. Therefore, the self-standing $\text{Li}_{1.2}\text{Mn}_{0.6}\text{Ni}_{0.2}\text{O}_2$ /graphene membrane electrode with high initial coulombic efficiency, rate capability and cycling stability is very potential as a cathode toward high performance Li-ion battery. This work may also provide a new method to improve the electrochemical performance of LROs through tuning the oxygen redox process during cycling.

Conflicts of interest

There are no conflicts to declare.

Acknowledgements

This work was supported by the National Basic Research Program of China (973 Program) (No. 2013CB934001), National Natural Science Foundation of China (No. 51575030) and Natural Science Foundation of Beijing, China (No. 2174075).

Notes and references

- 1 J. W. Choi and D. Aurbach, *Nat. Rev. Mater.*, 2016, **1**, 16013.
- 2 W. Li, X. Liu, H. Celio, P. Smith, A. Dolocan, M. Chi and A. Manthiram, *Adv. Energy Mater.*, 2018, 1703154.
- 3 F. Fu, Q. Wang, Y. P. Deng, C. H. Shen, X. X. Peng, L. Huang and S. G. Sun, *J. Mater. Chem. A*, 2015, **3**, 5197–5203.
- 4 C. Yang, X. Zhang, J. Huang, P. Ao and G. Zhang, *Electrochim. Acta*, 2016, **196**, 261–269.
- 5 M. M. Thackeray, S. H. Kang, C. S. Johnson, J. T. Vaughey, R. Benedek and S. A. Hackney, *J. Mater. Chem.*, 2007, **17**, 3112–3125.
- 6 K. A. Jarvis, Z. Deng, L. F. Allard, A. Manthiram and P. J. Ferreira, *Chem. Mater.*, 2011, **23**(16), 3614–3621.
- 7 H. Koga, L. Croguennec, M. Menetrier, K. Douhil, S. Belin, L. Bourgeois, E. Suard, F. Weill and C. Delmas, *J. Electrochem. Soc.*, 2013, **160**, A786–A792.
- 8 M. Sathiya, K. Ramesha, G. Rousse, D. Foix, D. Gonbeau, A. S. Prakash, M. L. Doublet, K. Hemalatha and J. M. Tarascon, *Chem. Mater.*, 2013, **25**, 1121–1131.
- 9 B. Song, H. Liu, Z. Liu, P. Xiao, M. O. Lai and L. Lu, *Sci. Rep.*, 2013, **3**, 3094.
- 10 K. Jarvis, C. C. Wang, M. Varela, R. R. Unocic, A. Manthiram and P. J. Ferreira, *Chem. Mater.*, 2017, **29**, 7668–7674.
- 11 L. Mu, R. Lin, R. Xu, L. Han, S. Xia, D. Sokaras, J. Steiner, T. C. Weng, D. Nordlund and M. M. Doeff, *Nano Lett.*, 2018, **18**, 3241–3249.
- 12 B. Xu, C. R. Fell, M. Chi and Y. S. Meng, *Energy Environ. Sci.*, 2011, **4**, 2223–2233.
- 13 P. Oh, M. Ko, S. Myeong, Y. Kim and J. Cho, *Adv. Energy Mater.*, 2015, **4**, 1400631.
- 14 A. R. Armstrong, M. Holzapfel, k. P. Nová, C. S. Johnson, S. H. Kang, M. M. Thackeray and P. G. Bruce, *J. Am. Chem. Soc.*, 2006, **128**, 8694–8698.
- 15 N. Yabuuchi, K. Yoshii, S. T. Myung, I. Nakai and S. Komaba, *J. Am. Chem. Soc.*, 2011, **133**, 4404.
- 16 B. H. Song, H. W. Liu, Z. W. Liu, P. F. Xiao, M. O. Lai and L. Lu, *Sci. Rep.*, 2013, **3**, 12.
- 17 H. Liu, C. Y. Du, G. P. Yin, B. Song, P. J. Zuo, X. Q. Cheng, Y. L. Maa and Y. Z. Gao, *J. Mater. Chem. A*, 2014, **2**, 15640–15646.
- 18 J. Li, C. Zhan, J. Lu, Y. Yuan, R. Shahbazian-Yassar, X. Qiu and K. Amine, *ACS Appl. Mater. Interfaces*, 2015, **7**, 16040–16045.
- 19 R. P. Qing, J. L. Shi, D. D. Xiao, X. D. Zhang, Y. X. Yin, Y. B. Zhai, L. Gu and Y. G. Guo, *Adv. Energy Mater.*, 2016, **6**, 6.
- 20 J. J. Wang and X. L. Sun, *Energy Environ. Sci.*, 2012, **5**, 5163–5185.



- 21 R. Dominko, M. Bele, M. Gaberscek, M. Remskar, D. Hanzel, S. Pejovnik and J. Jamnik, *J. Electrochem. Soc.*, 2005, **152**, A607–A610.
- 22 D. W. Choi, D. H. Wang, I. T. Bae, J. Xiao, Z. M. Nie, W. Wang, V. V. Viswanathan, Y. J. Lee, J. G. Zhang, G. L. Graff, Z. G. Yang and J. Liu, *Nano Lett.*, 2010, **10**, 2799–2805.
- 23 X. F. Zhou, F. Wang, Y. M. Zhu and Z. P. Liu, *J. Mater. Chem.*, 2011, **21**, 3353–3358.
- 24 J.-Z. Kong, C.-L. Wang, X. Qian, G.-A. Tai, A.-D. Li, D. Wu, H. Li, F. Zhou, C. Yu, Y. Sun, D. Jia and W.-P. Tang, *Electrochim. Acta*, 2015, **174**, 542–550.
- 25 P. Oh, M. Ko, S. Myeong, Y. Kim and J. Cho, *Adv. Energy Mater.*, 2014, **4**, 1400631.
- 26 B. Song, M. O. Lai, Z. Liu, H. Liu and L. Lu, *J. Mater. Chem. A*, 2013, **1**, 9954–9965.
- 27 C. H. Lei, J. Bareño, J. G. Wen, I. Petrov, S. H. Kang and D. P. Abraham, *J. Power Sources*, 2008, **178**, 422–433.
- 28 J. Bréger, M. Jiang, N. Dupré, Y. S. Meng, S. H. Yang, G. Ceder and C. P. Grey, *J. Solid State Chem.*, 2005, **178**, 2575–2585.
- 29 E. Wang, C. Shao, S. Qiu, H. Chu, Y. Zou, C. Xiang, F. Xu and L. Sun, *RSC Adv.*, 2017, **7**, 1561–1566.
- 30 Z. Liu, A. Yu and J. Y. Lee, *J. Power Sources*, 1999, **81–82(s)**, 416–419.
- 31 J. Lin, D. Mu, Y. Jin, B. Wu, Y. Ma and F. Wu, *J. Power Sources*, 2013, **230**, 76–80.
- 32 W. Yan, M. A. Worsley, T. Pham, A. Zettl, C. Carraro and R. Maboudian, *Appl. Surf. Sci.*, 2018, 372–379.
- 33 G. An, *Mater. Res. Bull.*, 2011, **46**, 1323–1326.
- 34 C. M. Julien and M. Massot, *Mater. Sci. Eng., B*, 2003, **100**, 69–78.
- 35 J. X. Huang, B. Li, B. Liu, B. J. Liu, J. B. Zhao and B. Ren, *J. Power Sources*, 2016, **310**, 85–90.
- 36 K. C. Jiang, X. L. Wu, Y. X. Yin, J. S. Lee, J. Kim and Y. G. Guo, *ACS Appl. Mater. Interfaces*, 2012, **4**, 4858.
- 37 S. Stankovich, D. A. Dikin, R. D. Piner, K. A. Kohlhaas, A. Kleinhammes, Y. Jia, Y. Wu, S. T. Nguyen and R. S. Ruoff, *Carbon*, 2007, **45**, 1558–1565.
- 38 A. C. Ferrari, J. C. Meyer, V. Scardaci, C. Casiraghi, M. Lazzeri, F. Mauri, S. Piscanec, D. Jiang, K. S. Novoselov and S. Roth, *Phys. Rev. Lett.*, 2006, **97**, 187401.
- 39 J. McIntyre, N. K. Verma, R. J. Smith, C. Moore, H. Nerl, N. Mcevoy, N. Berner, I. McGovern, U. Khan and P. Lyons, *RSC Adv.*, 2016, **6**, 65299–65310.
- 40 F. D. Yu, L. F. Que, Z. B. Wang, Y. Xue, Y. Zhang, B. S. Liu and D. M. Gu, *J. Mater. Chem. A*, 2017, **5**, 9365–9376.
- 41 M. Sathiya, G. Rousse, K. Ramesha, C. P. Laisa, H. Vezin, M. T. Sougrati, M. Doublet, D. Foix, D. Gonbeau and W. Walker, *Nat. Mater.*, 2013, **12**, 827–835.
- 42 D. Yang, A. Velamakanni, G. Bozoklu, S. Park, M. Stoller, R. D. Piner, S. Stankovich, I. Jung, D. A. Field, C. A. Ventrice and R. S. Ruoff, *Carbon*, 2009, **47**, 145–152.
- 43 N. V. Kosova, I. P. Asanov, E. T. Devyatkina and E. G. Avvakumov, *J. Solid State Chem.*, 1999, **146**, 184–188.
- 44 V. R. Galakhov, M. Demeter, S. Bartkowski, M. Neumann, N. A. Ovechkina, E. Z. Kurmaev, N. I. Lobachevskaya, Y. M. Mukovskii, J. Mitchell and D. L. Ederer, *Phys. Rev. B: Condens. Matter Mater. Phys.*, 2002, **65**, 113102.
- 45 E. Beyreuther, S. Grafström, L. M. Eng, C. Thiele and K. Dörr, *Phys. Rev. B: Condens. Matter Mater. Phys.*, 2006, **81**, 155425.
- 46 M. Gracia, J. F. Marco, J. R. Gancedo, J. Ortiz, R. Pastene and J. L. Gautier, *J. Phys. Chem. C*, 2010, **114**, 12792–12799.
- 47 B. Song, Z. Liu, M. O. Lai and L. Lu, *Phys. Chem. Chem. Phys.*, 2012, **14**, 12875–12883.
- 48 D. Yang, A. Velamakanni, G. Bozoklu, S. Park, M. Stoller, R. D. Piner, S. Stankovich, I. Jung, D. A. Field and C. A. V. Jr, *Carbon*, 2009, **47**, 145–152.
- 49 W. E. Gent, K. Lim, Y. Liang, Q. Li, T. Barnes, S. J. Ahn, K. H. Stone, M. McIntire, J. Hong and J. H. Song, *Nat. Commun.*, 2017, **8**, 2091.
- 50 D. Wang, B. Ilias, G. Zhou and A. Khalil, *Adv. Funct. Mater.*, 2013, **23**, 1070–1075.
- 51 Y. Zou, X. Yang, C. Lv, T. Liu, Y. Xia, L. Shang, G. I. Waterhouse, D. Yang and T. Zhang, *Adv. Sci.*, 2016, **4**, 1600262.
- 52 D. Luo, S. H. Fang, L. Yang and S. Hirano, *J. Mater. Chem. A*, 2016, **4**, 5184–5190.
- 53 J. C. Dupin, D. Gonbeau, P. Vinatier and A. Levasseur, *Phys. Chem. Chem. Phys.*, 2000, **2**, 1319–1324.
- 54 A. Manthiram, Y. You, H. Celio, A. Dolocan and J. Li, *Angew. Chem., Int. Ed. Engl.*, 2018, 6480–6485.

